Fully Integrated Buck and Boost Converter as a High Efficiency, High-Power-Density Off-Line LED Driver

Guirguis Z. Abdelmessih, J. Marcos Alonso, Marco A. Dalla Costa, Yu-Jen Chen, and Wen-Tien Tsai

***Abstract*—In this article, a high-power-density off-line light-emitting diode (LED) driver is proposed. The proposed ac–dc driver is the novel integrated buck and boost converter (IBBC). Besides the high-power-density, the converter shows a high power factor (PF), and a low total harmonic distortion (THD). The IBBC is a two-stage driver that features just one controlled switch, which leads to high PF and low THD operation ensuring high efficiency, and size and cost reduction. Moreover, the switch current is minimized as it conducts the higher of the buck or boost converter, but not the addition of both as in other integrated converters. Moreover, for a further increase of the power-density, a magnetic integration is made by integrating the two inductors of both the buck and boost converters in one core. Thus, the proposed converter has been named as fully integrated buck and boost converter (FIBBC). In this paper, the IBBC is analyzed, and a design methodology is proposed. Also, this article presents a magnetic analysis of the novel FIBBC. In addition, a comparison between two prototypes is presented, one for the IBBC and another for the FIBBC, both of them supplying an LED luminaire of 46 V/ 0.575 A. The FIBBC shows a high PF equal to 0.994, very small THD of 10%, output current ripple of 6%, and efficiency of 92.62%, which represents a landmark on the efficiency of integrated converters.**

***Index Terms*—Fully integrated buck and boost converter (FIBBC), high efficiency light-emitting diodes (LEDs) driver, integrated converters, magnetic integration, off-line LED drivers, power factor correction.**

I. Introduction

LIGHT-EMITTING diodes (LEDs) were first developed in 1960s [1]. Nowadays, they have become one of the most popular lighting sources in a wide variety of applications. This is owing to the following advantages shown by the LEDs:

1) Longer lifetime, which is usually quoted as 25 000 to 50 000 h for a minimum flux of 70% of the initial flux (L70) [2]–[5].
2) Higher efficacy compared to other light sources, as it is claimed in [6] that the incandescent lamps efficacy ranges between 14 to 17 lm/W, fluorescent tubes 100 lm/W, high-pressure sodium lamps reach 120 lm/W; however, the new generation of LED will have an efficacy up to 250 lm/W even 300 lm/W, as stated in [7].
3) Other features such as a smaller size, fast response, robustness, reliability, and high color rendering index [8]–[14].

The only drawback of LEDs is that they cannot be connected directly to the mains. Thus, it is fundamental to drive the LEDs through a current-controlled power supply [1], [6], [15]–[17]. The aim of this driver is not only to drive the LEDs, but also to fulfill all required standards. Working with a luminary load, fulfilling the IEC 61000-3-2 Class C Standard [18] concerning the harmonic content in the input current becomes a must [19]. In addition, the power factor (PF) must be higher than the level specified by the U.S. Energy Star program [20].

Numerous types of drivers have been presented in the literature. Single-stage drivers are used as PF correction (PFC) stage and constant output current source simultaneously. Most commonly used single-stage drivers are based on the buck and flyback converters. Both show good output control with acceptable PFC for low and even medium power applications [21]–[23]. Concerning the flyback converter operating as a single-stage driver, to perform a PFC it must operate in discontinuous conduction mode (DCM). However, operating in DCM makes the electric stress high, resulting in higher switch losses, and the usage of higher rating devices. Thus, operating with a single-stage driver efficiency will be compromised to fulfill PF and total harmonic distortion (THD) standard requirements or vice versa. Thus, for the sake of a better performance, the two-stage LED drivers are proposed [23]–[29], in both connections cascaded and parallel. The first stage is dedicated to operate as a PFC stage with just one focus, which is to achieve as high PF as possible, and to provide a stable dc voltage to the second stage. While, the second stage duty is to operate as a PC stage, controlling the current going to the LED and trying to filter the low-frequency ripple as much as possible [30]. In the case of the parallel two-stage driver, one stage operates as a PC and PFC simultaneously, while the second operates as ripple cancelation stage [28]–[29]. Yet, having two

Manuscript received December 10, 2019; revised March 7, 2020; accepted April 26, 2020. Date of publication May 10, 2020; date of current version July 20, 2020. This work was supported in part by the Asturias Regional Government under Research Grant Severo Ochoa PA-17-PF-BP16151, in part by the Solid-State Lighting Systems Dept. ITRI Hsinchu, Taiwan, R.O.C., and in part by the Brazilian Government through CAPES/PRINT No. 41/2017, 88887.364657/2019-00, INCT-GD, CAPES Project 23038.000776/2017-54, CNPq Project 465640/2014-1, and FAPERGS Project 17/2551-0000517-1. Recommended for publication by Associate Editor S. C. Tan. *(Corresponding author: Guirguis Z. Abdelmessih.)*

Guirguis Z. Abdelmessih and J. Marcos Alonso are with the Electrical Engineering Department, University of Oviedo, Gijón, 33204 Asturias, Spain (e-mail: uo242517@uniovi.es; marcos@uniovi.es).

Marco A. Dalla Costa is with the Federal University of Santa Maria, Rio Grande do Sul 97105-900, Brazil (e-mail: marcodc@gedre.ufsm.br).

Yu-Jen Chen and Wen-Tien Tsai are with the Lighting Energy-Saving Department, Industrial Technology Research Institute Hsinchu, Hsinchu 31057, Taiwan (e-mail: itria70177@itri.org.tw; itria20152@itri.org.tw).

Color versions of one or more of the figures in this article are available online at https://ieeexplore.ieee.org.

Digital Object Identifier 10.1109/TPEL.2020.2993796

converters may decrease the total efficiency of the driver [23]. Therefore, many techniques are made in order to overcome this issue, by properly designing and optimizing each stage separately or even by applying additional soft-switching techniques such as zero-voltage-switching (ZVS) or zero-current-switching (ZCS) [31]. The main drawbacks of these drivers are the higher number of components, and the fact that it contains at least two controlled switches, which means two gate drivers and associated circuitry, thus producing bigger size and higher cost. Many solutions have been proposed, as working with single stage converters and try to fulfill the standard [32] or boosting up the efficiency of the two-stage converters [33]–[34]. However, these solutions always include additional complicated circuitry.

A promising solution to overcome the previously presented drawbacks is the integrated converters. Integrated converters operate similarly to a two-stage converter but using a single switch. This means lower switching losses and only one driving circuit. Therefore, it keeps the good operation of the two-stage structure while providing some of the advantages of single-stage converters [10]–[12], [34]–[39].

Power quality figures as PF and THD are overly important, however, power density and efficiency have the same relevance and, in specific applications, even higher. The passive components such as the magnetic and capacitive elements are the most bulky and lossy components in the converter. The two-stage converter has two inductive elements, which decrease both the efficiency and power density. A proposed solution is to integrate both inductive elements in one core. The integrated inductor has previously been proposed in the literature operating as coupled inductors for multichannel buck converter [40]–[45], multichannel boost converter [46], and differential rectifier/inverter [47], however, it has never been explored in integrated converters.

In this paper, a fully integrated buck and boost converter (FIBBC) is proposed to supply an LED luminary load of 26.5 W, providing high PF, low THD, low current ripple, high efficiency, and compact design. The operation of the converter is equivalent to two separate converters working in a cascaded mode and sharing frequency and duty cycle; at the input, a buck converter operating as a PFC stage and at the output, a boost converter operating as a power control (PC) stage. The first integration is made in the controlled switch, which is shared by both stages. The second integration is made in the magnetic components, as both inductors are sharing the same core. Thus, the proposed converter only includes two capacitors, four diodes, one ground-referenced controlled switch, and one magnetic component, thus featuring affordable low cost and good reliability.

This paper is organized as the following: in Section II the FIBBC is presented. Section III shows the operational principles of the proposed IBBC, as well as the converter analysis, the magnetic analysis, and the average model. The design procedure is illustrated in Section IV, while simulation and experimental results are shown in Section V. Finally, a brief conclusion of the contribution of this paper is presented.

II. Derivation of the Proposed FIBBC

As previously mentioned, the converter is operating as two converters (buck and boost) operating in a cascaded mode.

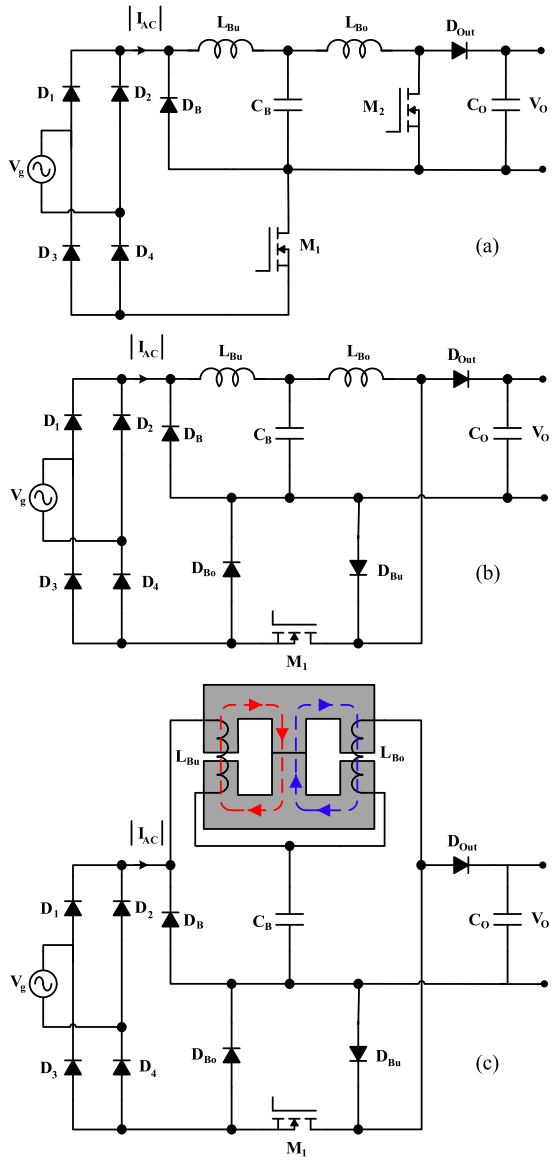

Fig. 1. (a) Electric diagram of a conventional cascade buck PFC and boost dc-dc LED driver. (b) Electric diagram of the integrated buck and boost converter. (c) Electric diagram and the magnetic structure of the fully integrated buck and boost converter.

Fig. 1(a) shows the electric diagram of the two converters before integration. The buck converter role is to operate as a PFC stage, so that it will be operating in DCM to behave as a resistive load at its input terminals [32], [33]. The boost converter role is to operate as a PC stage, in order to properly drive the LED. The benefits gained from this structure are the following: the buck converter will ensure a high PF and low THD as long as the bulk capacitor voltage is small enough [32], [33]; thus, having a boost converter at the output of the buck converter guarantees that the bulk capacitor voltage will be lower than the output voltage. This has a double benefit of ensuring good PF and the usage of a low voltage capacitor rating. Moreover, in order to assure good efficiency, the boost converter can be designed to operate with a low input–output voltage ratio. The topology does not include any transformers, which leads to a further increase of the efficiency, because winding losses and

losses associated with leakage inductance are minimized and avoided, respectively. The main disadvantage of this topology is the necessity of two switches, with two gate driving circuits and two controllers.

The integration of the two converters was the only solution to keep the same operating behavior and features, simultaneously avoiding one of the two switches. Fig. 1(b) shows the electric diagram of the integration of the buck and boost converters, named as integrated buck and boost converter (IBBC) [48]. The input buck converter is made up of L_{Bu}, D_B, D_{Bu}, C_B, and M_1, while the output boost converter is made up of the following components: L_{Bo}, D_{Out}, D_{Bo}, C_O, and M_1.

For the sake of higher power density and efficiency, the FIBBC is proposed. Fig. 1(c) shows the electrical diagram and the magnetic structure of the FIBBC. In this case L_{Bu} and L_{Bo} will share the same magnetic core, for higher power-density. Moreover, the windings are arranged in order to generate a reverse direction in the central arm, which in return decreases the magnetic losses and increases the efficiency.

III. Analysis of the Proposed IBBC

A. Operation Principle of the IBBC Converter

Since the proposed converter is a single switch converter, there are only two main states: ON-state and OFF-state. However, the DCM operation of the buck and boost converters splits the OFF-state into three intervals. Fig. 2, and Fig. 3 illustrate the equivalent circuits, and the main current waveforms within a high-frequency switching period, respectively.

Interval I represents the period where the switch is in turn-ON mode. When the switch is ON both converters are operating and both inductors have current passing through them. Later on, the switch is turned OFF. Starting by Interval II, which represents the period where the two inductors are de-energizing. i_{Bu} is the current passing through the buck inductor and charging the bulk capacitor, while i_{Bo} is the current discharging the bulk capacitor and passing through the boost inductor, going to the output. Interval III is the case when one of the two inductors current reaches zero and the other one is still conducting. Fig. 2(c) shows interval III for the case of the buck inductor current reaches zero, while the boost inductor current is still conducting. Finally, interval IV represents the period when all currents inside the converter are equal to zero. However, concerning the current going to the LED, it is continuous owing to the output capacitor presence.

It must be noted that the conduction of diodes D_{Bu} and D_{Bo}will be determined according to the value of the buck current and the boost current. Fig. 4 shows a simplified equivalent model for the switch and two diodes. If the buck current i_{Bu} is higher than the boost current i_{Bo}, then D_{Bu} will conduct the difference between the two currents, while D_{Bo} will not conduct, and the current passing through M_1 will be i_{Bu}. In the case that i_{Bo} is higher than i_{Bu}, the reverse will occur, D_{Bo} will conduct the difference between the two currents, while D_{Bu} will not conduct, and the current passing through M_1 will be i_{Bo}. Fig. 5 shows the converter currents. As shown in the figure, the buck current is sinusoidal, while the current of the boost is nearly

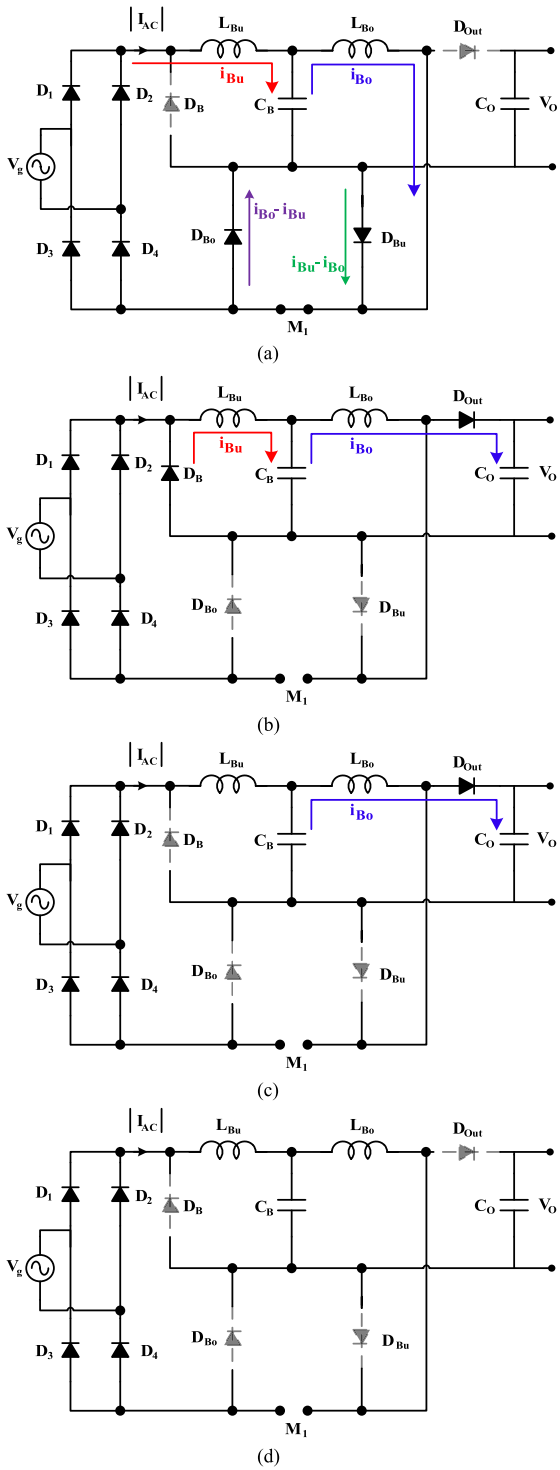

Fig. 2. Equivalent circuits of the IBBC operating in DCM. (a) Interval I: $0 < t < DT_s$. (b) Interval II: $DT_s < t < t1$. (c) Interval III: $t1 < t < t2$. (d) Interval IV: $t2 < t < T_s$.

constant in amplitude. Thus, the conduction of the two diodes will start by D_{Bo} then D_{Bu} at the buck peak value, and finally D_{Bo}. Moreover, one of these diodes can be eliminated if the design makes the buck peak current to remain below the boost peak current. Thus, D_{Bu} will never conduct and in return one diode can be eliminated.

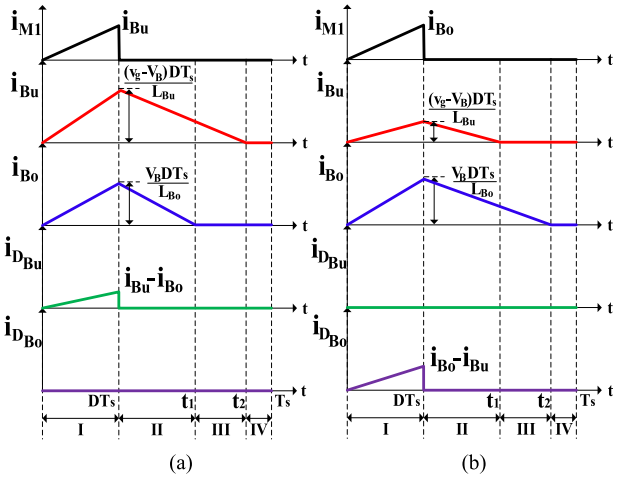

Fig. 3. Main current waveforms of the IBBC operating in DCM, within a high-frequency switching period. (a) When $i_{\mathrm{Bu}} > i_{\mathrm{Bo}}$ around the peak line voltage. (b) When $i_{\mathrm{Bu}} < i_{\mathrm{Bo}}$ for low values of the line voltage.

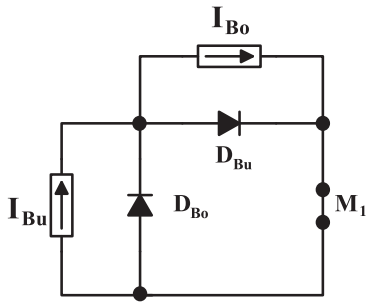

Fig. 4. Equivalent circuit for the operation of M_1.

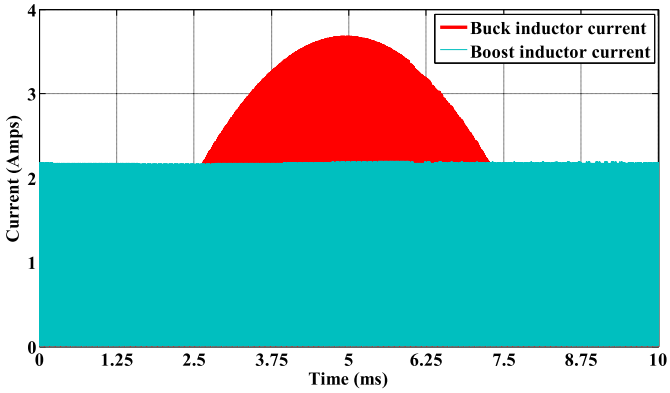

Fig. 5. Current of both buck and boost inductors.

As illustrated in the operational principle of the IBBC, the converter shows great advantages; the main switch handles less current, as it conducts only the higher between the buck current and the boost current, but not the addition of both. The losses are thus distributed among controlled switch and diodes, which is good because diodes behave as better switches than MOSFETs. Furthermore, the two diodes are not conducting continuously; they are operating in a complementary mode, so that only one of them conducts at a time. Moreover, it conducts the difference of the two converter currents not even the full magnitude of one of them.

B. Mathematical Analysis

In the following, the analysis of the currents in the converter is performed to obtain the important design equations, when both stages buck and boost operate in DCM. For the sake of simplicity, the analysis will consider the converter in its ideal state. An ideally sinusoidal line voltage waveform will be considered as input voltage, expressed as $v_g(t) = V_g \sin(2\pi f_l t)$.

The peak value of the buck current can be expressed as

$$\begin{aligned} i_{\mathrm{Bupeak}} &= \frac{D}{f_s L_{\mathrm{Bu}}} \left(v_{\mathrm{AC_{Bridge}}} - V_B \right) \\ &= \frac{D \left(V_g \left| \sin\left(2\pi f_l t\right) \right| - V_B \right)}{f_s L_{\mathrm{Bu}}} \end{aligned} \tag{1}$$

where L_{Bu} is the buck inductance, f_s is the switching frequency, D is the duty cycle, and V_B is the bulk capacitor voltage.

Concerning the boost current, it can be expressed as

$$I_{\mathrm{Bopeak}} = \frac{V_B D}{f_s L_{\mathrm{Bo}}} \tag{2}$$

where L_{Bo} is the boost inductance.

Regarding the operation of the converter, full DCM operation has to be guaranteed. Hence, a study of the boundaries is made in order to design the inductive elements. Thus, both buck and boost converters will behave as a resistive load at their inputs. The equivalent resistance value of the buck converter can be expressed as

$$R_g = \frac{2 L_{\mathrm{Bu}} f_s}{D^2}. \tag{3}$$

While the value of the boost input resistance is given as

$$R_{\mathrm{Bo}} = \frac{2 L_{\mathrm{Bo}} f_s}{D^2 \left(1 + \frac{V_B}{V_O - V_B} \right)} \tag{4}$$

where V_O is the output voltage.

The mean input power can then be calculated as

$$P_g = I_B V_B \tag{5}$$

where I_B is the buck inductor current.

As found in [33] the buck inductor current can be calculated as

$$I_B = \frac{V_g}{R_g} \left[\frac{1}{2m} \left(1 - \frac{2}{\pi} \sin^{-1} m \right) - \frac{\sqrt{1-m^2}}{\pi} \right] \tag{6}$$

where $m = V_B / V_g$ is the ratio between the bulk capacitor voltage to the peak line voltage.

Substituting (3) and (6) into (5), the following expression for the input power is found:

$$P_g = \frac{V_g V_B D^2}{2 L_{\mathrm{Bu}} f_s} \left[\frac{1}{2m} \left(1 - \frac{2}{\pi} \sin^{-1} m \right) - \frac{\sqrt{1-m^2}}{\pi} \right] \tag{7}$$

Concerning the boost power delivered to the output, it can be expressed as

$$P_{\mathrm{Bo}} = \frac{V_B^2}{R_{\mathrm{Bo}}} = \frac{D^2 V_B^2 \left(1 + \frac{V_B}{V_O - V_B}\right)}{2 L_{\mathrm{Bo}} f_s}. \tag{8}$$

Regarding the output power, it can be found using the equivalent resistance of the LED is

$$P_{\mathrm{Out}} = \frac{V_O^2}{R} \tag{9}$$

where R is the equivalent resistance of the LED load given by the ratio between LED voltage and current.

Concerning the voltage ratio of the FIBBC it can be split into two parts. First, the voltage ratio of the buck converter is given as

$$\frac{V_B}{V_g} = \frac{R_{\mathrm{Bo}}}{R_g}\left[\frac{1}{2m}\left(1 - \frac{2}{\pi}\sin^{-1} m\right) - \frac{\sqrt{1-m^2}}{\pi}\right]. \tag{10}$$

Second, the voltage ratio for the boost converter is given as

$$\frac{V_o}{V_B} = \frac{1 + \sqrt{1 + \frac{4D^2}{K_{\mathrm{bo}}}}}{2} \tag{11}$$

where K_{bo} is given as

$$K_{\mathrm{bo}} = \frac{2 L_{\mathrm{bo}} f_s}{R}. \tag{12}$$

Combining both (1) and (11) by substituting the value of the boost equivalent resistance in (5), an expression for the voltage ratio of the FIBBC operating as dc–dc converter is

$$\frac{V_o}{V_g} = \frac{2R}{R_g\left(1 + \sqrt{1 + \frac{4D^2}{K_{\mathrm{bo}}}}\right)} \times \left[\frac{1}{2m}\left(1 - \frac{2}{\pi}\sin^{-1} m\right) - \frac{\sqrt{1-m^2}}{\pi}\right]. \tag{13}$$

C. Magnetic Analysis

In this section, the magnetic analysis for the conventional two-separated cores and the integrated inductors is made to study if there will be any change in the operation, and for a better comparison between the two techniques. Fig. 6(a) shows the two equivalent magnetic circuits in the case of two separated inductors: the one on the left corresponds to the buck inductor and the one on the right corresponds to the boost inductor. The equivalent magnetic circuit of the integrated inductor is shown in Fig. 6(b). The right outer arm corresponds to the boost inductor, and the left outer arm corresponds to the buck inductor.

The integrated inductor is implemented by using a PQ core type. However, the analysis is also valid for the EE core type and the EFD core types, using the geometric parameters of the corresponding core. The design is made so that the flux from one inductor does not interact and affect the operation of the other inductor. For doing that, the design of the integrated inductor is made by putting the gaps in the outer arms, so that the reluctances of the outer arms are significantly higher than the reluctance of the center arm. Thus, the flux generated by each inductor goes to

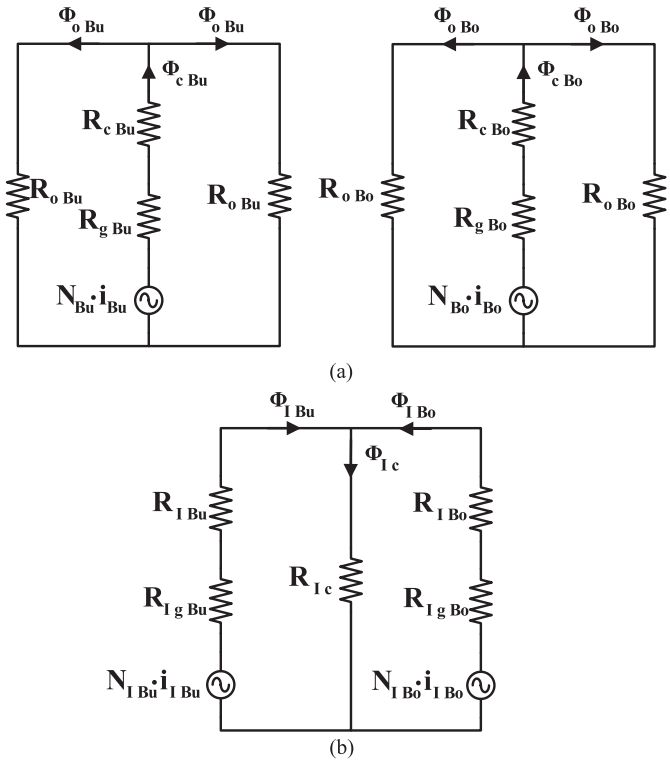

Fig. 6. Equivalent magnetic circuits. (a) Left side is the buck inductor, while the right side is the boost inductor. (b) The integrated inductor buck and boost.

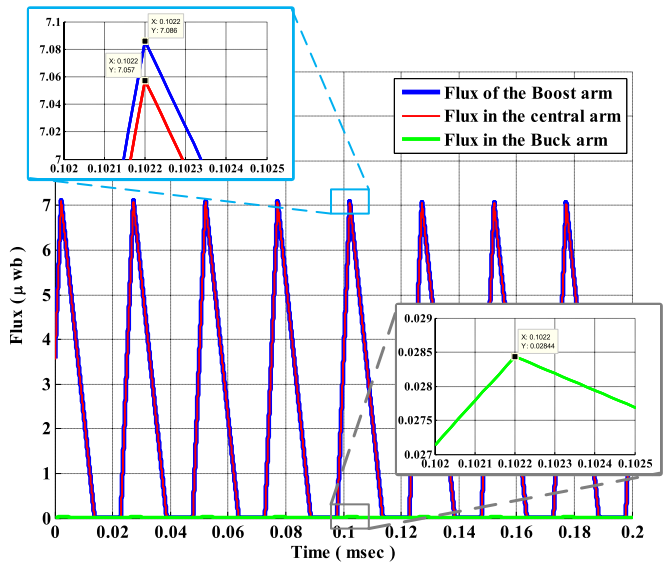

Fig. 7. Flux in the integrated core with deactivated buck MMF; the flux in the boost arm (in blue), the flux in the central arm (in red), and the flux in the buck arm (in green).

the center arm so that they do not affect each other. A simulation is made using the magnetic circuit presented in Fig. 6(b). The simulation is run one time removing the source representing the magneto-motive force (MMF) of the buck inductor, and another time while removing the source representing the MMF of the boost inductor. Fig. 7 shows the flux at the three arms of the integrated core in the case of deactivating the MMF of

the buck inductor and testing only the sharing percentages of the boost inductor flux. As shown in the figure, 99.5% of the flux goes through the center arm. Thus, in this paper, it will be approximated that there is no interference between the two inductors and none of the previously demonstrated equations and operation of the IBBC will change in the case of the FIBBC.

In order to solve the equivalent circuits presented in Fig. 6, the following parameters are found. The flux generated by the winding is given as

$$\Phi = \frac{NI}{R_e} \tag{14}$$

where Φ is the flux, N is the number of turns of the winding, I the current through the winding, and R_e is the reluctance of the core.

The reluctance of the core is given as

$$R_e = \frac{l}{\mu\mu_r A} \tag{15}$$

where l is the length of the flux path, A is the cross-section area of the core, μ is the air permeability, μ_r is the core material permeability.

To estimate the number of turns of the inductors the following expression is used:

$$L = \frac{N^2}{R_e} \tag{16}$$

where L is the inductance of the winding.

The reluctance presented in (16) is the total reluctance of the flux path. Apply this to the magnetic circuit presented in Fig. 6(a) for the buck inductor, the total reluctance is found as

$$\begin{aligned} R_{\mathrm{Bu}_{\mathrm{total}}} &= R_{C\ \mathrm{Bu}} + R_{g\ \mathrm{Bu}} + (R_{O\ \mathrm{Bu}} // R_{O\ \mathrm{Bu}}) \\ &= R_{C\ \mathrm{Bu}} + R_{g\ \mathrm{Bu}} + \frac{R_{O\ \mathrm{Bu}}}{2} \end{aligned} \tag{17}$$

where $R_{C\ \mathrm{Bu}}$ is the reluctance of the center arm of the buck inductor, $R_{g\ \mathrm{Bu}}$ is the air gap reluctance of the buck inductor, and $R_{O\ \mathrm{Bu}}$ is the reluctance of the outer arm of the buck inductor.

As an approximation, the reluctance of the core is neglected compared to the air gap reluctance. Thus, the number of turns of the buck inductor is calculated as

$$N_{\mathrm{Bu}} = \sqrt{L_{\mathrm{Bu}} R_{g\ \mathrm{Bu}}}. \tag{18}$$

Following the same procedure, the number of turns of the boost inductor is calculated as

$$N_{\mathrm{Bo}} = \sqrt{L_{\mathrm{Bo}} R_{g\ \mathrm{Bo}}}. \tag{19}$$

Concerning the integrated core, the magnetic circuit will be split into two parts. Furthermore, the outer arm path is neglected since 99.5% of the flux goes to the center arm. The total reluctance of the flux path of the buck inductor is given as

$$R_{I\ \mathrm{Bu}_{\mathrm{total}}} = R_{I\ C} + R_{I\ \mathrm{Bu}} + R_{I\ g\ \mathrm{Bu}} \tag{20}$$

where $R_{I\ C}$ is the reluctance of the center arm, $R_{I\ \mathrm{Bu}}$ is the reluctance of the outer arm of the buck inductor, $R_{I\ g\ \mathrm{Bu}}$ is the reluctance of the air gap of the buck inductor.

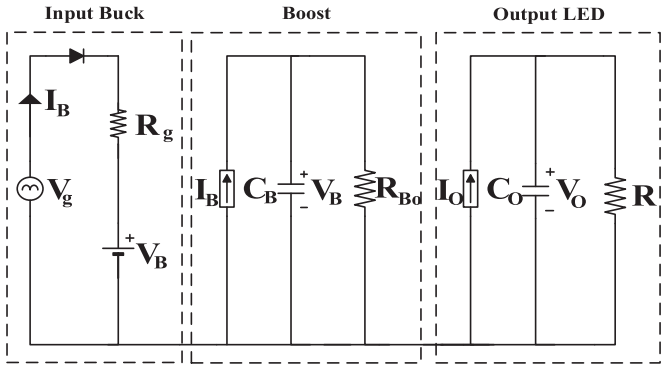

Fig. 8. Average model of the proposed FIBBC LED driver.

Applying the same approximation, the reluctance of the core is neglected compared to the reluctance of the air gap. Thus, the number of turns of the buck and boost inductors in the integrated core is given by the following expressions, respectively:

$$N_{I\ \mathrm{Bu}} = \sqrt{L_{\mathrm{Bu}} R_{I\ g\ \mathrm{Bu}}} \tag{21}$$

$$N_{I\ \mathrm{Bo}} = \sqrt{L_{\mathrm{Bo}} R_{I\ g\ \mathrm{Bo}}} \tag{22}$$

Concerning the values of the inductors, the selection is made under one constraint. As the value of the inductance increases, the peak value of the current presented in (1), and (2) decreases and in return a reduced devices rating is achieved. However, this increase is limited by the DCM mode of operation. First, the buck inductance is chosen in order to have a boundary conduction mode (BCM) at the peak value of the input voltage. Later, the critical value of the boost converter is given as

$$L_{\mathrm{Bo}_{\mathrm{crit}}} = \frac{RD(1-D)^2}{2f_s}. \tag{23}$$

D. Average Model

For better illustration of the converter operation, an average model is developed as shown in Fig. 8. The average model is useful in terms of understanding the power flow in the converter. As well as it is a faster way to check, by simulation, the magnitude of the voltages and currents in all elements without considering the high-frequency switching effect. The values of the buck and boost resistances used in the model are given by (3) and (4), respectively.

IV. Design Procedure of the Laboratory Prototype

Using the previously determined equations and the average model illustrated in Fig. 8, two designs are made to supply an LED luminaire of 46 V/ 575 mA, resulting in 26.5 W of output power. The line voltage is 110 V_{rms} and the line frequency is 60 Hz. First step in the design is to select the values of the inductors using the boundary conditions presented in (21) and (22). The values of the buck inductance and the boost inductance are 125 and 70 μH, respectively. Later, two designs are made for the inductors.

The first design is made for the case of the two separate cores for the two inductors. The number of turns is calculated so that

the magnetic loss is designed to be equal to the copper losses in the windings. Thus, the number of turns selected for the buck and boost inductances are 20 and 15, respectively. Using these values and the values of the core dimensions in the flux and reluctances equation, the equivalent circuit parameters in Fig. 6(a) are found.

To have a fair comparison between both standalone and integrated core versions, the number of turns of the boost inductor in the integrated core is designed to give the same flux density in the outer arms as that in the standalone boost inductor. Using (24), the maximum value of the flux density in the standalone boost inductor is calculated as

$$B_{\max} = \frac{L_{\mathrm{Bo}} \times I_{\max}}{A_e \times N_{\mathrm{Bo}}} \tag{24}$$

where L_{Bo} is the boost inductance and equal to 70 μH, $I_{\max}$ the maximum current in the boost inductor obtained from the simulation is equal to 2 A, A_e is the effective area of the central arm found in the datasheet of the PQ26/20 equal to 112 mm^2. Thus, the maximum value of the flux in the individual boost inductor $B_{\max}$ is found to be equal to 82 mT.

After having the value of the maximum flux density in the standalone core, the same procedure is repeated but this time for the integrated core. Applying the same procedure once again using (24), but using the effective cross-section area of the outer arm of the PQ32/20 chosen for the integrated core, which is equal to 88 mm^2, the number of turns is found to be 20.32. Thus, the number of turns of the boost inductor in the integrated core of 20 is chosen.

Concerning the buck inductor number of turns, it is calculated to have a flux density component at switching frequency equal to the boost inductor flux density at switching frequency. So, (24) is used with different inductance value 125 μH, and the value of the buck inductor current component at switching frequency 0.891 A, and the boost flux density component at the switching frequency equal to 34.27 mT. Thus, the number of turns found to be equal to 38.68, so a value of 40 turns was selected. Using these values and the values of the integrated core dimensions in the flux and reluctances equation, the equivalent circuit parameters in Fig. 6(b) are found.

The volume of the separate core equals to 10 145 mm^3, while the volume of the integrated core equals to 14 467 mm^3. Thus, the integrated design shows a reduction in the size of the magnetic component by 28.5%. Table I shows the values of the prototype components.

The IC used for the control is the LD7838. Fig. 9 shows the detailed schematic diagram of the laboratory prototype in both aspects: power and control. As a standalone driver, the power of the IC should come from the driver itself. The control IC has a built-in high-voltage startup system just by connecting it with a high resistance to the converter just after the bridge. Later on, the power is taken from a fourth winding added to the integrated core. The controller IC shows great advantages such as constant output current regulation and dimming capability. The control is made by adding a series resistance to the switch to obtain a voltage signal to the control IC. The series resistance can be calculated from the equations presented in [49]. Furthermore, as shown in Fig. 9 the two inductors are coupled in one core,

TABLE I
COMPONENTS OF LABORATORY PROTOTYPE

Component	Value
EMI Filter Inductor	*2.58 mH*
EMI Filter Capacitor	*68 nF*
Buck Inductance standalone L_{Bu}	*PQ26/20/PC44,* L_{Bu} = 125 μH, N_{Bu} = 20, g = 0.5 mm
Boost Inductance standalone L_{Bo}	*PQ26/20/PC44,* L_{Bo} = 70 μH, N_{Bo} = 15, g = 0.5 mm
Integrated Inductor	*PQ32/20/PC44,* L_{Bu} = 125 μH, $N_{l\,Bu}$ = 40, L_{Bo} = 70 μH, $N_{l\,Bo}$ = 20, $g_{l\,Bu}$ = 1 mm, $g_{l\,Bo}$ = 0.5 mm
Bulk Capacitor	470 µF, 50 V
Output Capacitor	470 µF, 63 V
M_1	SPA07N60C3
Bridge Diodes	DB156S
D_B & D_{Bu}& D_{Bo}	MURS260T3G
D_{OUT}	STPS3150

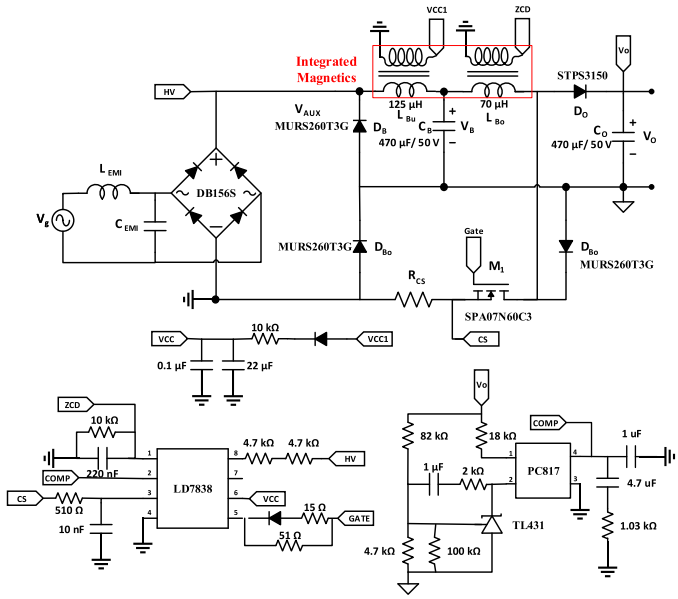

Fig. 9. Schematic diagram of the laboratory prototype.

simultaneously with two additional windings. The first winding is used as a supply for the control circuitry, while the second winding is used to give a signal for the current in the converter.

A great feature shown by the FIBBC is the low voltage of the bulk capacitor. The presence of the boost at the output of the integrated converter ensures a bulk capacitor voltage lower than the output voltage. This feature increases the power density of the FIBBC, as the used capacitor will be much smaller in size compared to any other technique.

V. SIMULATION AND EXPERIMENTAL RESULTS

As mentioned above, the flux of both inductors goes to the center arm of the integrated inductor core. The orientation of the inductors is made so that both fluxes are in the opposite direction as shown in the magnetic structure illustrated in Fig. 1(c). Fig. 9 shows the result of the simulation carried out using the circuits

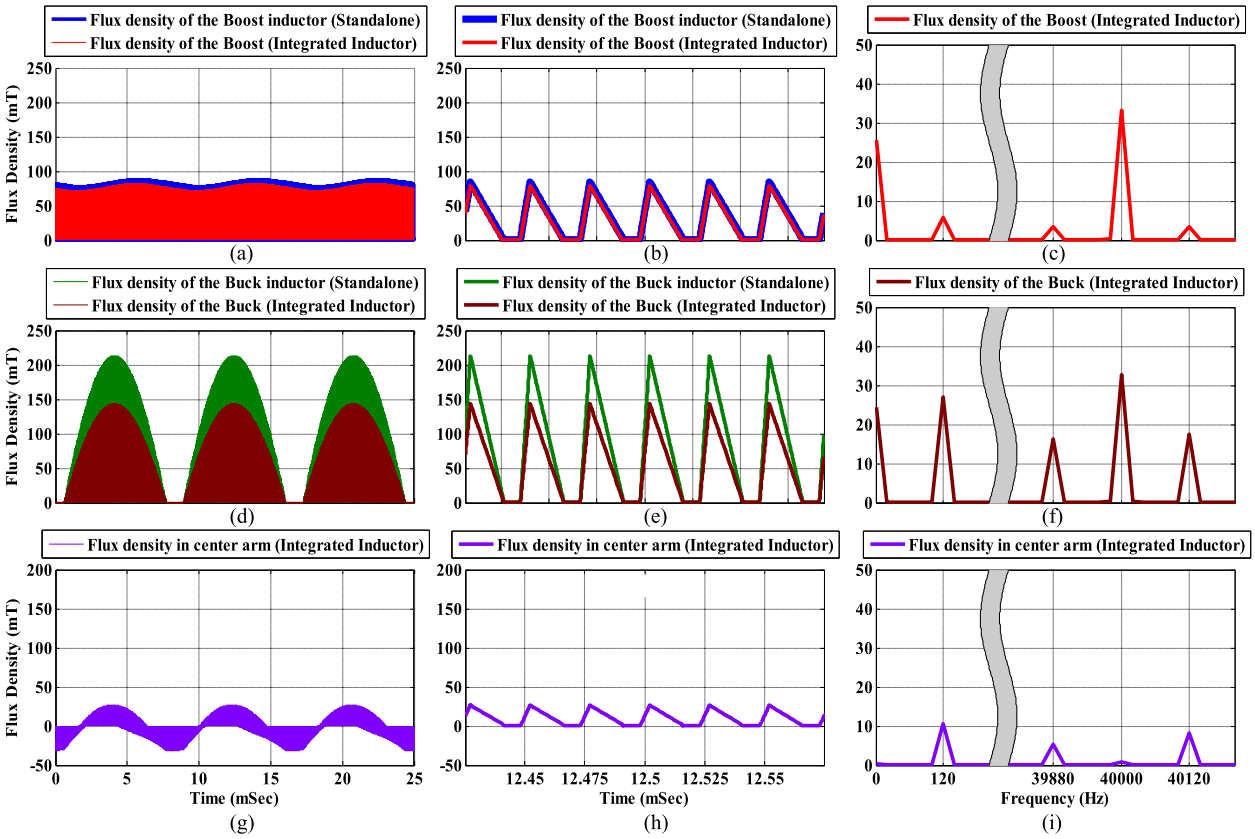

Fig. 10. Magnetic flux density in different parts of the core in both cases separate inductors and integrated inductors, in time and frequency domains.

presented in Fig. 6 together with the electrical representation of the full converter to measure the current through the inductors. Fig. 10(a) and (b) shows the magnetic flux density of the boost inductor in the case of standalone, and integrated inductor, respectively. As shown in Fig. 10(a) and (b), the flux is similar in both cases. Moreover, the design is made in order to have a peak value as close as possible for a fair comparison between both techniques. Fig. 10(c) shows the magnetic flux density of the boost arm in the integrated inductor in the frequency domain. It is composed mainly of two components, the dc component and another component at the switching frequency. The spectrum also shows some small components; one at double the line frequency, and two at the switching frequency plus and minus double the line frequency. Those are representing the low-frequency ripple. Fig. 10(d) and (e) shows the magnetic flux density of the buck inductor in the case of standalone and integrated inductor. As can be seen, the integrated core and separate cores show a similar flux. However, the flux of the integrated core is lower than the separate cores since it is designed to cancel the boost flux. Fig. 10(f) shows the magnetic flux density of the buck arm in the integrated inductor in the frequency domain. The FFT is applied to the magnetic flux waveform to show its component at each frequency. In the buck inductor, it has the same components as the boost inductor at dc and at the switching frequency. However, the components at the line frequency are higher due to the line frequency effect of the buck converter. Finally, Fig. 10(g) and (h) shows the magnetic flux density in the center arm in the integrated inductor. As shown in Fig. 10(g) and (h) the flux density in the center arm is much lower than the flux density in both cases the buck and boost arms, due to the opposite flux direction. Fig. 10(i) shows the magnetic flux density in the center arm of the integrated inductor in the frequency domain. In order to reduce magnetic losses, the design of the integrated inductor is made so that the buck and boost components at the switching frequency cancel each other. Fig. 10(i) shows that the center arm does not have any component at the dc and switching frequency. Unfortunately, the boost flux is not able to cancel the buck flux at double the line frequency; however, boost flux decreases it.

The integration of the magnetics will enhance the power density of the converter; however, the improvement of the efficiency is not clear. Thus, an estimation for the core losses in the case of the standalone cores and integrated core in both same and reverse direction of the flux in the center arm has been carried out. The losses are estimated using the data presented in the core datasheet [50]–[51], which provide the per volume losses at each frequency with respect to the flux density. In the following the procedures taken in order to estimate the core losses are described.

1) Using the magnetic model presented in Fig. 6 for the inductors in both cases, standalone and integrated core, the flux density at each part of the core is found as shown in Fig. 10.
2) The data presented in the datasheet of the per volume losses are for sine wave data. Thus, the waveforms of the

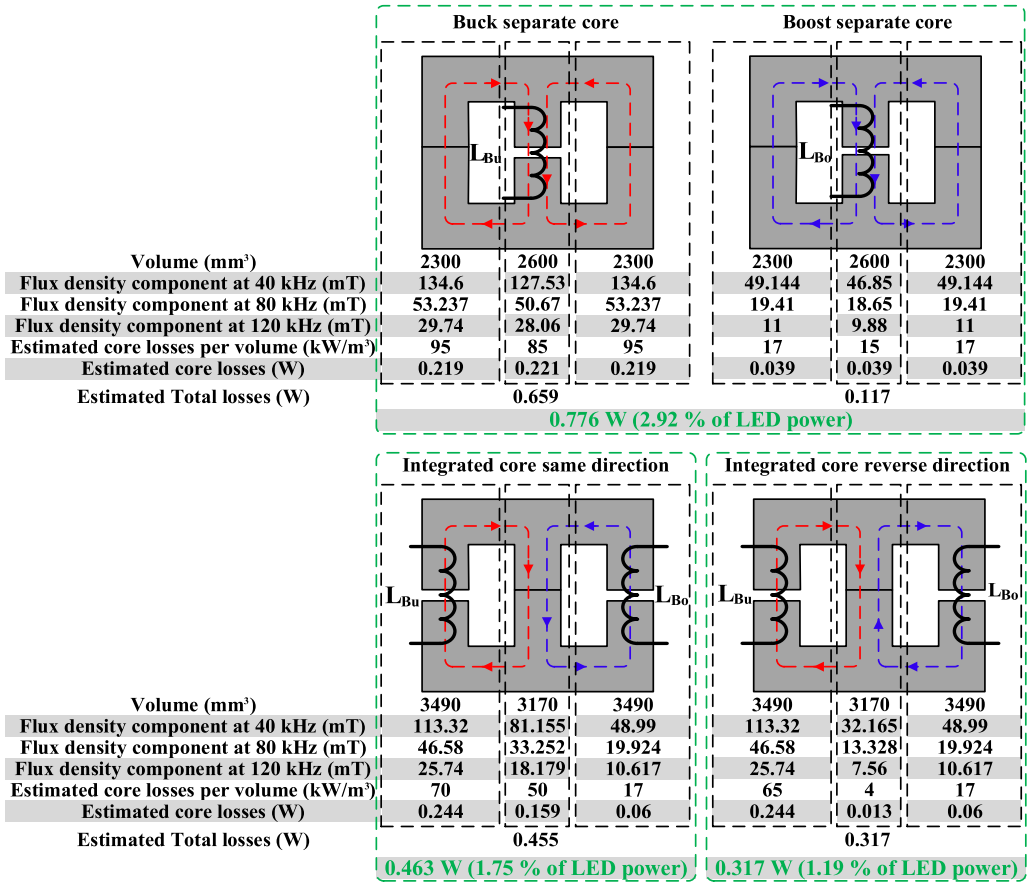

Fig. 11. Core losses estimation for the standalone cores, the integrated core in both same and reverse direction of the flux in the center arm.

flux density are analyzed using the FFT technique to find the sine component at each frequency.

3) Because of the double line-frequency ripple, the waveforms are modulated in amplitude. Therefore, there is usually a main component at the switching frequency and other component around it at the switching frequency plus and minus multiples of the double of the line frequency. In this analysis all these components are added and considered to be at the switching frequency.
4) The same occurs at multiples of the switching frequency. In this analysis up to the third harmonic is considered.
5) Using the flux density magnitude at each frequency and the data of the per volume losses, an estimation of the per volume losses value at each part of the converter is found.

Fig. 11 shows the data found by the analysis. As shown, due to the slightly decreased flux density and the volume reduction going from the two standalone cores to the integrated core (same direction), a reduction in the losses of 1.17% is achieved. Furthermore, using the reverse direction in the center arm a total reduction of 1.73% in the core losses is achieved.

The line voltage, as well as current waveform, is shown in Fig. 12. As shown in this figure, the current waveform is almost a pure sinusoidal waveform, which illustrates how the proposed technique ensures that the PF and the THD will be in their best conditions. Analyzing the input current waveform, the PF is 0.994 and the THD is 10%. Thus, the FIBBC shows a better

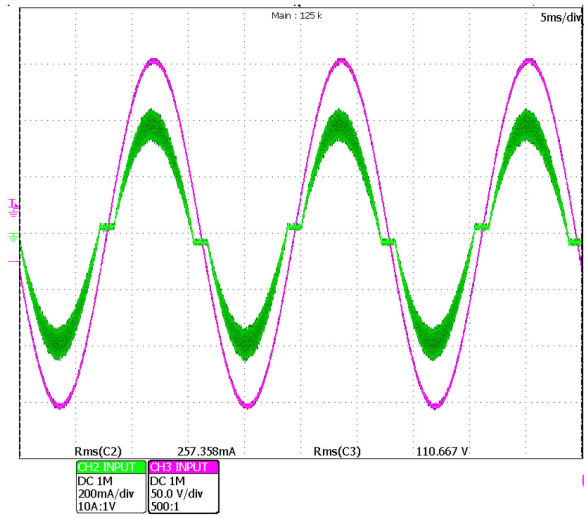

Fig. 12. Input current in green, and input sinusoidal voltage in red.

PF and THD compared to the IBBC. The efficiency is found to be 92.62%, which is a high-efficiency value considering that it is a low power application of 26.5 W. As per literature review, integrated converters show efficiency between 85% and 91%. It seems that the fully integrated converter will show higher efficiency than the conventional integrated converter.

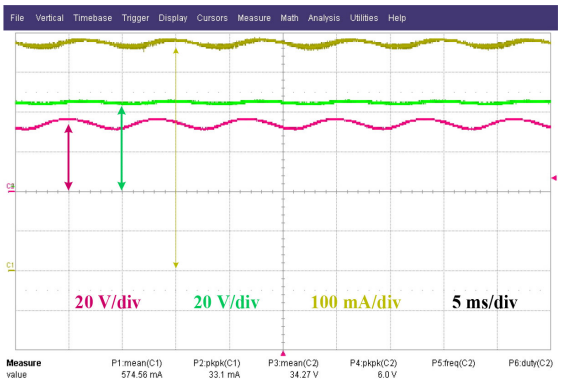

Fig. 13. Bulk voltage (red), output voltage (green), and output current (yellow).

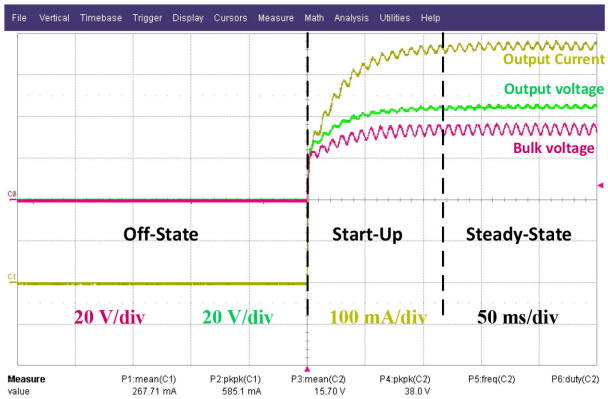

Fig. 14. Bulk voltage (red), output voltage (green), and output current (yellow).

Fig. 13 shows the bulk capacitor voltage, the output voltage, and the output current. As it can be seen, the current is controlled at the desired value, thus demonstrating the good operation of the converter. The low-frequency ripple of the output current is in the range of 6% of the rated current, which means that the converter fulfills the IEEE flicker recommendation [52].

Fig. 14 shows the output voltage and current, and the bulk voltage at start-up. As can be seen, the control is perfectly working as voltage and currents are reaching the desired values of 46 V and 0.575 A. Moreover, the converter shows a smooth and fast start-up process.

Fig. 15 shows the voltage across the MOSFET switch (in green), and the current through it (in yellow). As shown in the figure, the voltage across the switch is relatively low compared to other integrated converters, which explains the high efficiency of this converter. As shown in the voltage across the switch, a resonance can be observed at the end of the period, which is due to the nonconduction interval of the DCM operation of the converter. The current passing through the switch is in this case the buck current, as it is higher than the boost current.

Fig. 16 shows the two inductors currents. As shown in the figure, the boost inductor current is operating in BCM, which proves the accuracy of the used (23) in the design. Moreover, the buck inductor current is not entering the CCM operation, which demonstrates the correct design of the converter.

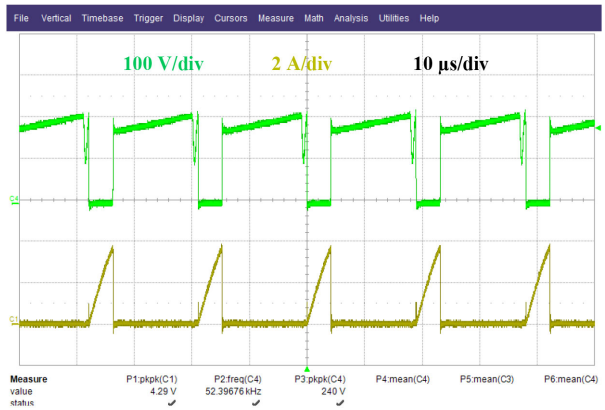

Fig. 15. Voltage across the MOSFET switch (in green), and the current through it (in yellow).

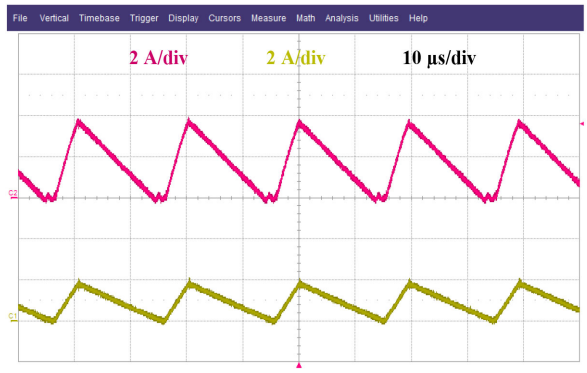

Fig. 16. Buck inductor current (in red), and the boost inductor current (in yellow).

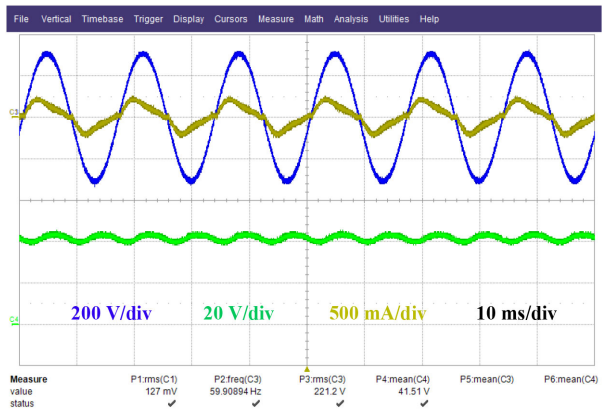

Fig. 17. Input voltage (blue), bulk voltage (green), and input current (yellow).

Fig. 17 shows the converter operating in high input voltage to prove the universal operation. It is operating with input voltage 220 V and rated power. The converter is perfectly operating, with even higher efficiency than as low line voltage, which equals 93.5%. One drawback is the distortion of the current waveform, as the electromagnetic interference (EMI) filter is designed for the 110 V operation. However, a great benefit shown by the converter is that the bus capacitor voltage will not increase too much, as it should be always below the output voltage. Thus, the

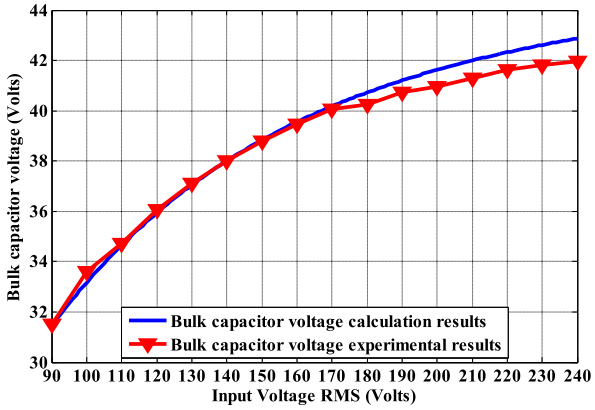

Fig. 18. The bus capacitor voltage with respect to input voltage, by calculations (blue), and from experimental results (red).

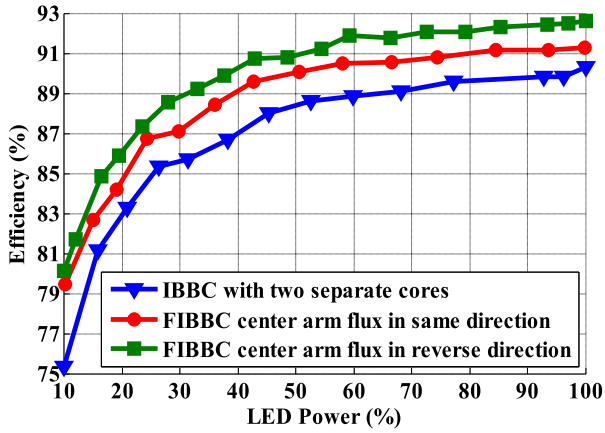

Fig. 20. IBBC and FIBBC efficiency concerning the dimming ratio.

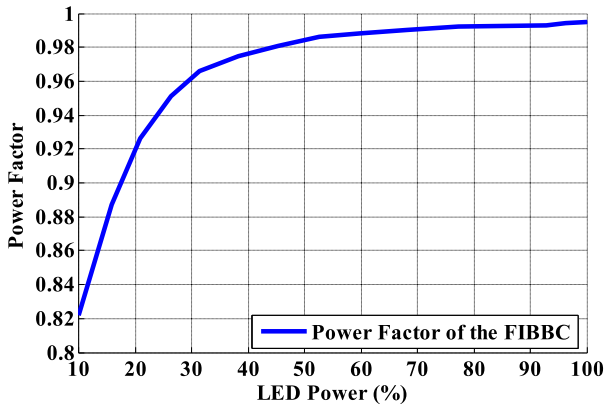

Fig. 19. Power factor of the FIBBC concerning the dimming ratio.

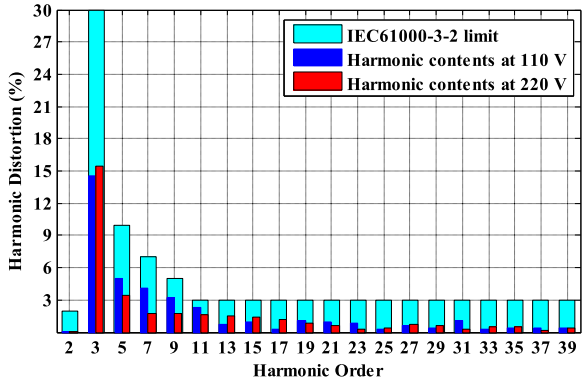

Fig. 21. Input current harmonic contents at both input voltages 110 and 220 V in comparison with the IEC 61000-3-2 limit.

PF is decreasing due to the distortion, but not so much because the ratio between the bus capacitor voltage and input voltage decreases. The PF is found to be 0.98 with a current THD equal to 13%.

In order to prove the advantage shown by the converter, which is the small increase of the bus capacitor voltage all over the universal input voltage range, Fig. 18 is presented. Fig. 18 shows the bulk capacitor voltage with respect to the input voltage, mathematically and with experimental results. As shown in the figure with an increase of 150 V in the input voltage, the bus capacitor voltage increases by only 10 V.

Fig. 19 shows the PF of the FIBBC concerning the dimming ratio. The used dimming in this technique is the analog dimming, by changing the duty cycle of the controlled switch. As can be seen, the PF is above 0.99 till 70% of rated power. Moreover, the PF is above 0.9 for a dimming ratio equal to 0.2 of the rated power.

Fig. 20 shows the efficiency of the IBBC and FIBBC with the central arm flux in the same and reverse direction, as a function of the dimming ratio. As can be seen, the efficiency is improved going from the IBBC to the FIBBC, even with the central flux in the same direction. The reason of the efficiency improvement of the FIBBC is the less flux density included in the core, and the effective volume decrease which in return decreases the magnetic losses as previously illustrated in the core losses analysis. Integrating the two magnetic elements does not guarantee an efficiency improvement. As by [42] the integration of the two inductors usually decreases the efficiency. However, the claim that the integration of two inductors will increase or decrease the efficiency cannot be generalized, because it depends mostly on the application and on the design. Yet, what can be generalized is the size reduction. Concerning this specific application both size reduction and efficiency increase were achieved. Furthermore, by reversing the polarity of the boost inductor to have the flux of the boost in the center arm in the opposite direction of the flux of the buck, the efficiency is boosted even more.

Fig. 21 shows the harmonics breakdown of the input current for both input voltages, 110 and 220 V, compared to the IEC61000-3-2 limit. As shown in the figure the converter fulfills the standard limits over the universal input voltage range.

Further enhancement in the power density of the driver is achieved by the manufactured prototypes. These prototypes are implemented using reduced magnetic components, the EFD 25 for the separate cores, and the EFD 30 for the integrated core. Fig. 22 shows the two manufactured PCBs, the IBBC in Fig. 22(a), and the FIBBC in Fig. 22(b). The manufactured PCBs are very compact showing a total volume of 56 cm^3.

TABLE II
COMPARISON AMONG THE PROPOSED CONVERTER AND THE FOUND IN LITERATURE INTEGRATED CONVERTER [12], [35], [38], [53]–[57]

Integrated Double Buck-Boost [12]	**Integrated Buck and Flyback [35][38]**	**Integrated buck-boost and class E resonant [53]**	**Integrated Flyback and class E resonant [54]**	**Integrated boost and LLC resonant [55-56]**	**Integrated buck-boost and LLC resonant [57]**	**Proposed Fully integrated Buck and Boost**
1 Switch	*1 Switch*	*1 Switch*	*1 Switch*	*2 switches*	*2 switches*	*1 Switch*
2 inductors	*1 inductor*	*3 inductors*	*2 inductors*	*1 inductor*	*2 inductors*	*1 coupled inductor*
0 transformer	*1 transformer*	*1 transformer*	*2 transformers*	*1 transformer*	*2 transformers*	*0 transformer*
3 diodes	*4 diodes, can be optimized to 3.*	*6 diodes*	*4 Diodes*	*4 diodes*	*6 diodes*	*4 diodes, can be optimized to 3.*
2 capacitors.	*2 capacitors.*	*4 Capacitors*	*4 Capacitors*	*6 capacitors*	*5 Capacitors*	*2 capacitors*
720 V, for output voltage 200 V.	*Around 700 V, for output voltage 48 V.*	*Around 600 V, for output voltage 50 V.*	*Around 500 V, for output voltage 50 V.*	*Around 750 V, for output voltage 50 V.*	*Around 400 V, for output voltage 50 V.*	*Between 160 V to 300 V for output voltage 46 V.*
Between 240 to 366 V.	*60 % of input voltage.*	*160 V.*	*Around 200 V.*	*Around 430 V.*	*Around 420 V.*	*35 V.*
No electric isolation.	*Electric isolation*	*Electric isolation*	*Electric isolation*	*Electric isolation.*	*Electric isolation*	*No electric isolation.*
Universal operation can be achieved.	*Universal operation can be achieved.*	*Universal operation can be achieved.*	*Universal operation can be achieved.*	*Universal operation can be achieved.*	*Universal operation can be achieved.*	*Universal operation can be achieved.*
Efficiency of 85 %, at rated power 70 W.	*Efficiency of 80 %, at rated power 100 W. Can be boosted to achieve 89 %. [29]*	*Efficiency of 90.8%, at rated power 100 W.*	*Not mentioned*	*Efficiency of 91.1 %, at rated power 100 W.*	*Efficiency of 91 %, at rated power 100 W.*	*Efficiency of 92.6 %, at rated power 26.5 W.*
High power factor of 0.96.	*High power factor of 0.96.*	*High power factor of 0.99.*	*Not mentioned*	*High power factor of 0.98.*	*High power factor of 0.995.*	*High power factor of 0.994.*

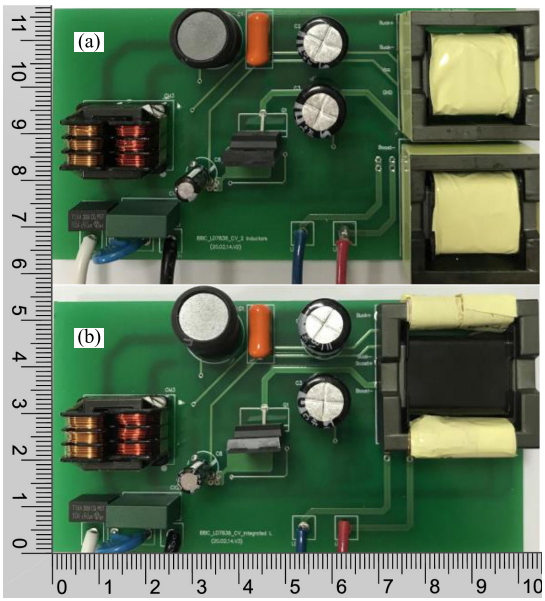

Fig. 22. Manufactured prototypes. (a) The IBBC prototype, and in (b) the FIBBC prototype.

The reduction in the magnetic component in the case of the EFD cores reaches 28%. The total reduction in the magnetic components is equal to 3.5 cm^3 which represent 6.25% of the total PCB size.

Finally, a comprehensive comparison with the integrated converters found in the literature is shown in Table II. The following converters were found: the integrated double buck boost converter [12], the integrated buck flyback converter [35], [38], the integrated buck-boost with class E resonant converter [53], the integrated flyback with resonant converter [54], the integrated boost and LLC resonant converter [55]–[56], and the integrated buck-boost and LLC resonant converter [57]. As shown in Table II, the proposed driver shows better features or at least similar than all integrated converters, except that it has no electric isolation.

VI. CONCLUSION

This article presents a novel converter that features high-efficiency, high PF, and low THD to be far below standards limitations at all dimming ranges. Additionally, the proposed topology does not require any complex circuitry neither advanced sensors nor any coupled inductors or transformers, which means that a spike-less operation is ensured, as well as minimized winding losses. Regarding the power components, the proposed topology offers all these features by using only one controlled switch, which additionally handles low current. Two extra diodes are added; however, these diodes are not continuously conducting so the losses do not harm the converter efficiency excessively. For further increase of the power density, a magnetic integration is made by integrating the two inductors of both the buck converter and boost converter in one core.

Finally, two prototypes working at a universal input range, and 46 V output, driving an LED luminary of 26.5 W, have been designed to illustrate the application of the derived characteristics. Experimental results have proven that the harmonic content of the input current of the FIBBC is equal to 10%, with a PF of 0.994, so that the converter meets all standards. The FIBBC shows a high efficiency of 92.62%, compared to 90.5% of efficiency shown by the IBBC. Moreover, the FIBBC shows an improvement of 2% in the efficiency within all the dimming range. Furthermore, the FIBBC shows a size reduction in the magnetic component compared to the IBBC of 28.35%.

REFERENCES

[1] J. Bullough, "Lighting answers: LED lighting systems," in *Proc. Nat. Lighting Product Inf. Program*, Lighting Research Center, vol. 7, no. 3. Troy, N.Y.: Rensselaer Polytechnic Institute, 2003.

[2] Cree LED lamps, 2016. [Online]. Available: http://creebulb.com/products

[3] GE LED lamps, 2016. [Online] Available: http://catalog.gelighting.com/lamp/led-lamps/

[4] Philips lighting, 2016. [Online] Available: http://www.lighting.philips.com/main/prof

[5] J. M. Alonso, *LED Lighting and Drivers*" Seattle, WA, USA: Amazon KDP, 2019.

[6] A. Barroso, P. Dupuis, C. Alonso, B. Jammes, L. Seguier, and G. Zissis, "A characterization framework to optimize LED luminaire's luminous efficacy," in *Proc. IEEE Industry Appl. Soc. Annu. Meeting*, Addison, TX, 2015, pp. 1–8.

[7] R. Jaschke and K. F. Hoffmann, "Higher light efficacy in LED-Lamps by lower LED-Current," in *Proc PCIM Europe Int. Exhib. Conf. Power Electron.*, Intelligent Motion, Renewable Energy and Energy Management, Nuremberg, Germany, 2016, pp. 1–5.

[8] R. L. Lin, Y. C. Chang, and C. C. Lee, "Optimal design of LED array for single-loop CCM buck–boost LED driver," *Proc. IEEE Trans. Ind. Appl.*, vol. 49, no. 2, pp. 761–768, Mar./Apr. 2013.

[9] D. Camponogara, G. F. Ferreira, A. Campos, M. A. Dalla Costa and J. Garcia, "Offline LED driver for street lighting with an optimized cascade structure," *Proc. IEEE Trans. Ind. Appl.*, vol. 49, no. 6, pp. 2437–2443, Nov./Dec. 2013.

[10] G. Z. Abdelmessih and J. M. Alonso, "A new active hybrid-series-parallel PWM dimming scheme for off-line integrated LED drivers with high efficiency and fast dynamics," in *Proc. IEEE Ind. Appl. Soc. Annu. Meeting*, Portland, OR, 2016, pp. 1–8.

[11] G. Z. Abdelmessih, J. M. Alonso, and M. A. Dalla Costa, "Analysis, design, and experimentation of the active hybrid-series-parallel PWM dimming scheme for high-efficient off-line LED drivers," *IET Power Electr.*, vol. 12, no. 7, pp. 1697–1705, Jun. 2019.

[12] J. M. Alonso, J. Vina, D. G. Vaquero, G. Martinez, and R. Osorio, "Analysis and design of the integrated double buck–boost converter as a high-power-factor driver for power-LED lamps," *IEEE Trans. Ind. Electron.*, vol. 59, no. 4, pp. 1689–1697, Apr. 2012.

[13] R. L. Lin, J. Y. Tsai, S. Y. Liu, and H. W. Chiang, "Optimal design of LED array combinations for CCM single-loop control LED drivers," *IEEE Trans. Emerg. Sel. Topics Power Electron.*, vol. 3, no. 3, pp. 609–616, Sep. 2015.

[14] R. A. Pinto, M. R. Cosetin, A. Campos, M. A. Dalla Costa, and R. N. do Prado, "Compact emergency lamp using power LEDs," *IEEE Trans. Ind. Electron.*, vol. 59, no. 4, pp. 1728–1738, Apr. 2012.

[15] R. A. Pinto, J. M. Alonso, M. S. Perdigão, M. F. da Silva, and R. N. do Prado, "A new technique to equalize branch currents in multiarray LED lamps based on variable inductors," *IEEE Trans. Ind. Appl.*, vol. 52, no. 1, pp. 521–530, Jan./Feb. 2016.

[16] Y. Wang, J. M. Alonso, and X. Ruan, "A review of LED drivers and related technologies," *IEEE Trans. Ind. Electron.*, vol. 64, no. 7, pp. 5754–5765, Jul. 2017, doi: 10.1109/TIE.2017.2677335.

[17] H. van der Broeck, G. Sauerlander, and M. Wendt, "Power driver topologies and control schemes for LEDs," in *Proc. Proc Twenty-Second Annu. IEEE Appl. Power Electron. Conf. Expo.*, Anaheim, CA, USA, 2007, pp. 1319–1325.

[18] *Electromagnetic Compatibility (EMC) - Part 3-2: Limits for Harmonic Current Emissions*, IEC Standard IEC 61000-3-2, 2005.

[19] G. G. Pereira, M. A. Dalla Costa, J. M. Alonso, M. F. De Melo, and C. H. Barriquello, "LED driver based on input current shaper without electrolytic capacitor," *IEEE Trans. Ind. Electron.*, vol. 64, no. 6, pp. 4520–4529, Jun. 2017.

[20] "ENERGY star program requirements for solid state lighting luminaries, version 1.3," U.S. Environ. Protection Agency, U.S. Dept. Energy, Washington, DC, USA, Rep. 1.3, 2010.

[21] J. W. Kim, J. P. Moon, and G. W. Moon, "Analysis and design of a single switch forward-flyback two-channel LED driver with resonant-blocking capacitor," *IEEE Trans. Power Electron.*, vol. 31, no. 3, pp. 2314–2323, Mar. 2016.

[22] F. Zhang, J. Ni, and Y. Yu, "High power factor AC–DC LED driver with film capacitors," *IEEE Trans. Power Electron.*, vol. 28, no. 10, pp. 4831–4840, Oct. 2013.

[23] Y. Wang, J. M. Alonso, and X. Ruan, "A review of LED drivers and related technologies," *IEEE Trans. Ind. Electron.*, vol. 64, no. 7, pp. 5754–5765, Jul. 2017.

[24] S. Moon, G. B. Koo, and G. W. Moon, "A new control method of interleaved single-stage flyback AC–DC converter for outdoor led lighting systems," *IEEE Trans. Power Electron.*, vol. 28, no. 8, pp. 4051–4062, Aug. 2013.

[25] H. Dong, X. Xie, L. Jiang, Z. Jin and X. Zhao, "An electrolytic capacitorless high power factor LED driver based on a "one-and-a-half stage" forward-flyback topology," *IEEE Trans. Power Electron.*, vol. 33, no. 2, pp. 1572–1584, Feb. 2018.

[26] I. Castro, A. Vazquez, M. Arias, D. G. Lamar, M. M. Hernando, and J. Sebastian, "A review on flicker-free AC–DC LED drivers for single-phase and three-phase AC power grids," *IEEE Trans. Power Electron.*, vol. 34, no. 10, pp. 10035–10057, Oct. 2019.

[27] H. Wu, S. Wong, C. K. Tse, S. Y. R. Hui, and Q. Chen, "Single-phase LED drivers with minimal power processing, constant output current, input power factor correction, and without electrolytic capacitor," *IEEE Trans. Power Electron.*, vol. 33, no. 7, pp. 6159–6170, Jul. 2018.

[28] S. Wang, X. Ruan, K. Yao, S. Tan, Y. Yang, and Z. Ye, "A flicker-free electrolytic capacitor-less AC–DC LED driver," *IEEE Trans. Power Electron.*, vol. 27, no. 11, pp. 4540–4548, Nov. 2012.

[29] Y. Yang, X. Ruan, L. Zhang, J. He, and Z. Ye, "Feed-forward scheme for an electrolytic capacitorless AC/DC LED driver to reduce output current ripple," *IEEE Trans. Power Electron.*, vol. 29, no. 10, pp. 5508–5517, Oct. 2014.

[30] F. Zhang, J. Ni, and Y. Yu, "High power factor AC–DC LED driver with film capacitors," *IEEE Trans. Power Electron*., vol. 28, no. 10, pp. 4831–4840, Oct. 2013.

[31] Y. Wang, Y. Guan, D. Xu, and W. Wang, "A CLCL resonant DC/DC converter for two-stage LED driver system," *IEEE Trans. Ind. Electron.*, vol. 63, no. 5, pp. 2883–2886, May 2014.

[32] Y. Wang, J. Huang, W. Wang, and D. Xu, "A single-stage single-switch LED driver based on class-E converter," *IEEE Trans. Ind. Appl.,* vol. 52, no. 3, pp. 2618–2626, May/Jun. 2016.

[33] Y. Wang, Y. Guan, D. Xu, and W. Wang, "A CLCL resonant DC/DC converter for two-stage LED driver system," *IEEE Trans. Ind. Electron.*, vol. 63, no. 5, pp. 2883–2891, May 2016.

[34] G. Z. Abdelmessih, J. M. Alonso and M. A. Dalla Costa, "Loss analysis for efficiency improvement of the integrated buck–flyback LED driver," *IEEE Trans. Ind. Appl.*, vol. 54, no. 6, pp. 6543–6553, Nov./Dec. 2018.

[35] Gacio, D., Alonso, J. M., Garcia, J., Campa, 1., Crespo, M. J., and RicoSecades, M., "PWM series dimming for slow-dynamics HPF LED drivers: The high-frequency approach, " *IEEE Trans. Ind. Electron.*, vol. 59, no. 4, pp. 1717–1727, Apr. 2012

[36] Gacio, D., Alonso, J. M., Calleja, A. J., Garcia, J., and Rico-Secades, M., "A universal-input single-stage high-power-factor power supply for HBLEDs based on integrated buck-flyback converter, " in *Proc. Twenty-Fourth Annu. IEEE Appl. Power Electron. Conf. Expo.*, Feb. 2009, pp. 570–576.

[37] J. M. Alonso, M. A. Dalla Costa, and C. Ordiz, "Integrated buck-flyback converter as a high-power-factor off-line power supply," *IEEE Trans. Ind. Electron.*, vol. 55, no. 3, pp. 1090–I 100, Mar. 2008

[38] J. Garcia, M. A. Dalla-Costa, J. Cardesin, J. M. Alonso, and M. RicoSecades, "Dimming of high-brightness LEOs by means of luminous flux thermal estimation," *IEEE Trans. Power Electron.*, vol. 24, no. 4, pp. 1107–1114, Apr. 2009.

[39] G. Z. Abdelmessih, J. M. Alonso, and W. Tsai, "Analysis and experimentation on a new high power factor off-line LED driver based on interleaved integrated buck flyback converter," *IEEE Trans. Ind. Appl.*, vol. 55, no. 4, pp. 4359–4369, Jul./Aug. 2019, doi: 10.1109/TIA.2019.2910785

[40] P. L. Wong, Peng Xu, P. Yang, and F. C. Lee, "Performance improvements of interleaving VRMs with coupling inductors," *IEEE Trans. Power Electron.*, vol. 16, no. 4, pp. 499–507, Jul. 2001.

[41] P. Zumel, O. Garcia, J. A. Cobos, and J. Uceda, "Magnetic integration for interleaved converters," in *Proc. Eighteenth Annu. IEEE Appl. Power Electron. Conf. Expo.*, Miami Beach, FL, USA, 2003, vol. 2, pp. 1143–1149.

[42] Y. Yugang, Y. Dong, and F. C. Lee, "A new coupled inductors design in 2-phase interleaving VRM," in *Proc. IEEE 6th Int. Power Electron. Motion Control Conf.*, Wuhan, pp. 344–350, 2009.

[43] J. Li, C. R. Sullivan, and A. Schultz, "Coupled-inductor design optimization for fast-response low-voltage DC-DC converters," in *Proc. Seventeenth Annu*. IEEE Appl. Power Electron. Conf. Expo., Dallas, TX, USA, 2002, vol. 2, pp. 817–823 .

[44] H. Li, Z. Chen, and Y. Yang, "Application study of multi-phase coupled array integrated magnetic in VRM," in *Proc. 2nd Int. Symp. Power Electron. Distrib. Gener. Syst.*, Hefei, 2010, pp. 214–219.

[45] S. Lee, A. G. Pfaelzer, and J. D. van Wyk, "Comparison of different designs of a 42-V/14-V DC/DC converter regarding losses and thermal aspects," IEEE *Trans. Ind. Appl.,* vol. 43, no. 2, pp. 520–530, Mar./Apr. 2007.
[46] P. W. Lee, Y. S. Lee, D. K. W. Cheng, and X. C. Liu, "Steady-state analysis of an interleaved boost converter with coupled inductors," *IEEE Trans. Ind. Electron.*, vol. 47, no. 4, pp. 787–795, Aug. 2000.
[47] M. Wu, S. Li, S. Tan and S. Y. M. Wu, S. Li, S. Tan, and S. Y. Hui, "Optimal design of integrated magnetics for differential rectifiers and inverters," IEEE *Trans. Power Electron.,* vol. 33, no. 6, pp. 4616–4626, Jun. 2018.
[48] G. Z. Abdelmessih, J. M. Alonso, W. Tsai, and M. A. Dalla Costa, "High-efficient high-power-factor off-line LED driver based on integrated buck and boost converter," in *Proc. IEEE Ind. Appl. Soc. Annu. Meeting*, Baltimore, MD, USA, 2019, pp. 1–6.
[49] Leadtrend Technology Corporation "High power factor flyback LED controller with HV start-up," LD7838-DS-01 Nov. 2016. [Online]. Available: https:www.leadtrend.com.tw
[50] Mn-Zn Ferrite Cores for Switching Power Supplies PQ series Datasheet, Mar. 2014. [Online]. Available: https://product.tdk.com/info/en/catalog/datasheets/ferrite_mz_sw_pq_en.pdf
[51] Ferrite for Switching Power Supplies Datasheet, Jul. 2003, 002-01/20030729/e140
[52] A. Wilkins, J. Veitch and B. Lehman, "LED lighting flicker and potential health concerns: IEEE standard PAR1789 update," in *Proc. IEEE Energy Convers. Congr. Expo.*, Atlanta, GA, 2010, pp. 171–178.
[53] Y. Wang, J. Huang, W. Wang and D. Xu, "A single-stage single-switch LED driver based on integrated buck-boost circuit and Class E converter," in *Proc. IEEE Ind. Appl. Soc. Annu. Meeting*, Addison, TX, 2015, pp. 1–5.
[54] Y. Wang, Y. Qiu and D. Xu, "A single-stage LED driver based on resonant converter with low-voltage stress," in *Proc. IEEE Ind. Appl. Soc. Annu. Meeting*, Portland, OR, 2018, pp. 1–5.
[55] Y. Wang, Y. Guan, K. Ren, W. Wang, and D. Xu, "A single-stage LED driver based on BCM boost circuit and LLC converter for street lighting system," *IEEE Trans. Ind. Electron.*, vol. 62, no. 9, pp. 5446–5448, Sep. 2015.
[56] J. Ma, X. Wei, L. Hu and J. Zhang, "LED driver based on boost circuit and LLC converter," *IEEE Access*, vol. 6, pp. 49588–49600, 2018.
[57] Y. Wang, Y. Guan, J. Huang, W. Wang and D. Xu, "A single-stage LED driver based on interleaved buck–boost circuit and LLC resonant converter," *IEEE Trans. Emerg. Sel. Topics Power Electron.*, vol. 3, no. 3, pp. 732–741, Sept. 2015

Guirguis Z. Abdelmessih received the B.Sc. degree in electrical engineering from the University of Ain Shams, Cairo, Egypt, in 2013 and the M.Sc. degree in electrical energy conversion and power systems from the University of Oviedo, Gijón, Spain, in 2015. He is currently working toward the Ph.D. degree on "analysis and development of improved converters for LED drivers with special focus on efficiency and dimming" granted by the government of the Principality of Asturias, Spain under "Severo Ochoa" Program of Pre-doctoral Grants for Training in Research and University Teaching.

His research interests include light-emitting diodes (LED), LED drivers, dc/dc converters, ac/dc converters, PFC stages, dimming systems, renewable energy, and power systems.

J. Marcos Alonso received the M. Sc. and Ph. D. degrees both in electrical engineering from the University of Oviedo, Spain, in 1990 and 1994, respectively.

Since 2007, he is a full Professor with the Electrical Engineering Department, University of Oviedo. His research interests include lighting applications, dc-dc converters, power factor correction, resonant inverters and power electronics in general.

He has co-authored more than 400 journal and conference publications, including more than 100 publications in highly referenced journals. He holds seven Spanish patents.

Prof. Alonso was the recipient of nine IEEE awards.

He is an Associate Editor with the IEEE TRANSACTIONS ON POWER ELECTRONICS and *IEEE Journal on Emerging and Selected Topics on Power Electronics*. He was Chair of the IEEE IAS Industrial Lighting and Displays Committee (ILDC) for the term 2017–2018.

Marco A. Dalla Costa was born in Santa Maria, Brazil, in 1978. He received the B.S. and M.Sc. degrees from the Federal University of Santa Maria, Brazil, in 2002 and 2004, respectively, and the Ph.D. degree (with hons.) from the University of Oviedo, Gijón, Spain, in 2008, all in electrical engineering.

From 2008 to 2009, he was an Associate Professor with the Universidade de Caxias do Sul, Brazil. Since 2009, he is a Professor with the Federal University of Santa Maria, Brazil. He has coauthored more than 60 journal papers and more than 100 international conference papers, and holds two Spanish patents. His research interests include dc/dc converters, power factor correction, lighting systems, high-frequency electronic ballasts, discharge-lamp modeling, light-emitting-diode systems, renewable energy systems, solid state transformers, and visible light communication systems.

Dr. Dalla Costa is also the Technical Department Chair of the Manufacturing Systems Development and Applications Department (MSDAD) and Chair of the Industrial Lighting and Displays Committee (ILDC), both from the IEEE Industry Applications Society. He serves as a reviewer for several IEEE Journals and Conferences in the field of power electronics. He is an Associate Editor with the IEEE TRANSACTIONS ON INDUSTRIAL ELECTRONICS and also with the *IEEE Journal of Emerging and Selected Topics in Power Electronics*.

Wen-Tien Tsai was born in Pingtong, Taiwan, R.O.C., in 1984. He received the B.S. degree from Southern Taiwan University of Science and Technology, Tainan, Taiwan in 2006, and the M.S. degree from National Sun Yat-Sen University, Kaohsiung, Taiwan in 2008, respectively, all in electrical engineering.

He is currently a Senior Engineer with the Lighting Energy-Saving Department in Industrial Technology Research Institute, Hsinchu, Taiwan. His research is focused on power electronic converters and their applications on lighting technology including the LED lighting drivers, power factor correction, and integrated power converters.

Yu-Jen Chen was born in Taichung, Taiwan, in 1984. She received the B.S. degree from Chang Gung University, Tao-Yuan Taiwan in 2007, and the M.S. and Ph.D. degrees in electrical engineering from National Sun Yat-Sen University, Kaohsiung, Taiwan in 2009 and 2018, respectively, all in electrical engineering.

She is currently working with the Lighting Energy-Saving Department of Industrial Technology Research Institute, Hsinchu, Taiwan. Her research interests include switching-mode power supplies and their applications on LED lighting technology.